RSC Advances

ROYAL SOCIETY OF CHEMISTRY

www.rsc.org/advances

Highly enhanced dielectric strength and energy storage density in hydantoin@BaTiO$_3$–P(VDF-HFP) composites by a sandwich– structure

Hang Luo,[a] Dou Zhang*[a], Lu Wang,[a] Chao Chen,*[a] Jing Zhou[b] and Kechao Zhou[a]

[a] State Key Laboratory of Powder Metallurgy, Central South University, Changsha, Hunan 410083, China

[b] State Key Laboratory of Advanced Technology for Materials Synthesis and Processing, Wuhan University of Technology, Wuhan 430070, China

E-mail: dzhang@csu.edu.cn (D. Zhang) and pkhqchenchao@126.com (C. Chen)

Keywords: dielectric strength, energy storage, composites, P(VDF-HFP), sandwich– structure

Abstract

A sandwich–structured composite consisted of a pure poly(vinylidene fluoride-co-hexafluoropropylene) (P(VDF-HFP)) central layer and two $BaTiO_3$–P(VDF-HFP) neighboring layers was developed for high energy storage density. The sandwiched structure effectively enhanced dielectric properties and energy storage capacity of the composites. Breakdown strength and energy storage density of the composite with 35 vol% P(VDF-HFP) central layer reached 315 kV mm^{-1} and 5.22 J cm^{-3}, which were enhanced by 68% and 125% compared to 187 kV mm^{-1} and 2.32 J cm^{-3} of the single layer composite, respectively. The dielectric constant of the composites with sandwich–structure was approximately 3 times higher than the pure P(VDF-HFP) and the dielectric loss was as low as 0.026 at 1 kHz. These results demonstrated that the sandwich–structured ceramics/polymer composite was an effective way to produce high energy density composites.

2

Introduction

Dielectric materials are usually required to afford high energy density and low dielectric loss for the applications on advanced electronic devices and electric power systems, such as embedded capacitors, multilayer capacitors, and gate insulators in organic field effect transistors.[1-6] In general, the maximum energy density (U_{max}) of the dielectrics materials is defined as $U_{max} = 1/2\varepsilon_0\varepsilon_r E^2$, where ε_0 and ε_r are the dielectric constant of the vacuum and the relative dielectric constant of the materials, respectively, E is the applied electric field. It can be seen that the maximum energy storage density can be obtained by simultaneously increasing dielectric constant and breakdown strength.[7, 8] Polymer holds excellent insulativity, plasticity, the endurance of high electric field and low dielectric loss, but suffers from low dielectric constant (i.e. <10).[5, 9-11] Ferroelectric ceramics (e.g. $BaTiO_3$ (BT), $Pb(Zr, Ti)O_3$) have high dielectric constants, but show the disadvantages of relatively low dielectric strength and high dielectric loss.[12-16] During the past decades, a lot of attention were paid on introducing ferroelectric ceramic fillers to polymer matrix to produce high energy storage density composites, because the ceramics/polymer composites simultaneously combine high dielectric constant from the ceramic fillers and high dielectric strength, low dielectric loss as well as flexibility from the polymer matrix.[17-20] It is recognized that the ceramics/polymer composite is one of the most promising dielectric materials for the application on energy storage.[17, 18] However, unavoidable defects caused by agglomeration of ceramic particles in the composites and weak interfacial adhesion between inorganic ceramics and organic matrix would reduce the dielectric strength

3

and energy storage density of the composites. Furthermore, due to the significant difference of the dielectric properties between ceramic fillers and polymer matrix, there would be an uneven distribution of electric field in the composite, which would also lead to the reduction of the dielectric strength. In other words, the increased dielectric constant of the composite is often at the expense of the significant reduction of the breakdown strength.[3, 20, 21]

Recently, a large number of strategies have been sought to mitigate the reduction of the breakdown strength. (i) One of the strategies was chemical modification methods to prepare uniformly composite films based on homogeneous dispersion of ceramic fillers in polymer matrix and firm interfacial adhesion between ceramic fillers and polymer matrix.[22-24] Yang et. al. proposed core– shell structured polymer @ BT nanocomposites by *in-situ* polymerization on the surfaces of nanoparticles, resulting in high dielectric constant, low dielectric loss, and high energy storage density capability.[23] (ii) Some employed poly(vinylidene fluoride) (PVDF) and its copolymer as the polymer matrix to reduce the difference of dielectric properties between polymer matrix and ceramic fillers. PVDF and its copolymer are ferroelectric polymers, which have higher dielectric constant than other polymers.[25-30] (iii) Particular structures based on sandwich or multi–layers structure were proposed to maintain the dielectric strength as high as possible.[2, 3, 26] Specifically, an insulating layer was intercalated to the composites. Pure polymers or the nanocomposites with small amounts of ceramic nanofibers were usually selected as the insulating layer attributed to the relatively

high dielectric strength.[2, 3] Sun et. al., proposed a pure polymer interlayer between the carbon nanotubes/PVDF hybrid layers, resulting in high dielectric constant and low loss composites.[26] Hu et. al., achieved ultrahigh dielectric strength and energy storage density through introducing BT nanofibers–PVDF central layer to the BT nanoparticles–PVDF composites.[2, 3] It was observed that introducing interfacial buffer layers to the composite was an effective method to prepare high energy storage density dielectric materials. Since the tailored central layer in the sandwich or the multi–layers composites is so critical, however, the effects of the thickness of the central layer relative to the entire composites on the dielectric properties and the capacity of energy storage have been rarely reported.

In this paper, we developed sandwich–structured composites with various thicknesses of intercalated pure polymer layers in the BT–P(VDF-HFP) composites. BT nanoparticles were selected as the fillers in the outer layers to produce high dielectric constant.[14, 21] It was reported in our previous study that the P(VDF-HFP) composites with 50 vol% BT possessed relatively higher dielectric constant (see table S1 in ESI†).[31] Pure P(VDF-HFP) was employed as the central layer due to the relatively high breakdown strength and higher dielectric constant than other polymers.[25, 26] In particular, all of the BT nanoparticles were modified by a kind of water soluble hydantoin epoxy resin . The dielectric properties and energy storage density with the various thicknesses of the central layer composites were emphatically investigated. By contrast, the samples of pure P(VDF-HFP) polymer and BT–P(VDF-HFP) composite without central layer were also prepared. The modified

nanoparticles displayed homogeneous dispersion in polymer matrix and firm interfacial adhesion with the matrix. The sandwich–structured composites exhibited extremely low dielectric loss and significantly increased dielectric strength compared with the composites without central layer. Among the sandwich–structured composites, the energy storage density of the composites with 35 vol% pure polymer central layer increased to 5.22 J cm^{-3}, which was 2.25 times of the composite without central layer (2.32 J cm^{-3}). The findings of this research could provide a feasible approach to produce high energy storage density dielectric materials.
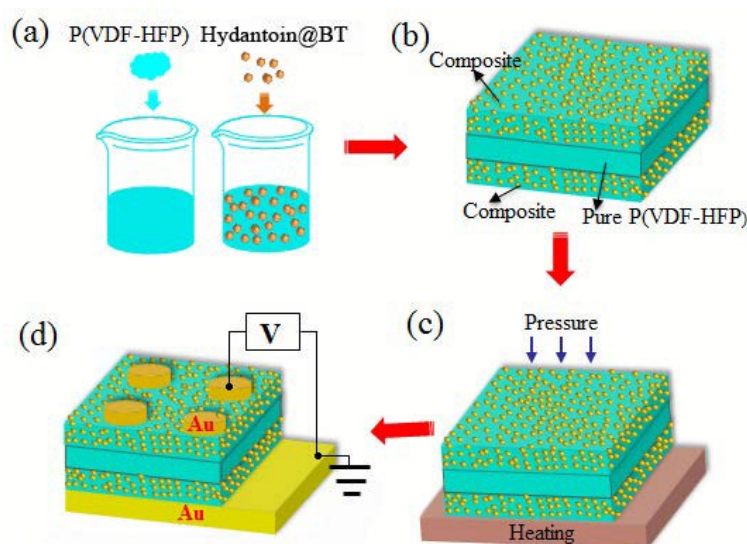
Fig. 1 Schematic illustration for (a) preparing P(VDF-HFP) solution and P(VDF-HFP) suspension with dispersed BT nanoparticles, (b) preparing the sandwich–structured composite, (c) the process of hot–pressing, (d) sputtering electrode for testing electric properties. V is defined as testing equipment.

Experimental

20 g of BT nanoparticles (Aladdin, 99%) were added into 100 ml of H_2O_2 (Sinopharm, China, 30 wt%) aqueous solution in an around–bottomed flask. The mixture was

sonicated for 30 min and reuxed at 106 °C for 6 h. The nanoparticles were recovered

by centrifugation at 9000 rpm for 5 min. The obtained BT nanoparticles were

thoroughly washed by deionized water and then dried under vacuum at 80 °C for 12 h.

Subsequently, 5 g of hydantoin epoxy resins (Wuxi Meihua Chemical co., LTD, 99%)

and moderate sulfuric acid were dissolved in deionized water, and mixed with 10 g of

H_2O_2 treated BT nanoparticles, followed by stirring and heating for 2h. 0.5 g of

dipropylenetriamine (TCI（Shanghai）, 99%) was added into the mixed suspension and

stirred at room temperature for 20 h, and then stirred at 80 °C for 2 h. The hydantoin

resin coated BT nanoparticles (hydantoin@BT) were recovered by centrifuging at

1000 rpm for 2 min, washed by deionized water thoroughly and finally dried under

vacuum at 80 °C for 12 h.

Samples were successfully prepared through simple solution–casting and hot–

pressing methods. Specifically, hydantoin@BT was ball–milled in *N*,

N-dimethylformamide (DMF) (Sinopharm, China) for 2 days, and mixed with

P(VDF-HFP) (Aldrich, pellets with less than 15% of HFP), ball–milled for another 5

days. The resultant suspension was casted onto a clean glass, then pure P(VDF-HFP)

solution, and BT/P(VDF-HFP) suspension were casted layer-by-layer onto the surface

of the samples. Afterwards, all of the samples were dried respectively at room

temperature and 80 °C for 12 h under vacuum to obtain sandwich–structured

composite sheets. The composite without central pure polymer layer and pure

P(VDF-HFP) polymer were prepared in a similar way. All of the dried composites

sheets were compressed into films at 200 °C under a pressure of about 15 MPa.

Circular gold electrodes with diameter of 2 mm were sputtered on one side of the film using a metal mask, and the other side was fully sputtered by gold electrode. The fabrication process of sandwich–structured hydantoin@BT–P(VDF-HFP) composites is shown in Fig. 1, which was included four sections. (a) Preparation P(VDF-HFP) solution and uniform hydantoin@BT/P(VDF-HFP) suspension. (b) Preparation the sandwich–structured hydantoin@BT–P(VDF-HFP) composite via a layer–by–layer tape casting method. Specifically, the uniform suspension with hydantoin@BT nanoparticles was casted onto a glass plate to form the first layer composite film, then, different thicknesses of central pure P(VDF-HFP) layer was obtained by different concentration of P(VDF-HFP) solution, the top–layer was also hydantoin@BT–P(VDF-HFP) composite. (c) The samples were compressed into compact films by hot–pressing. (d) The films were sputtered gold electrode for electrical property tests. In contrast, pure P(VDF-HFP) and single layer hydantoin@BT–P(VDF-HFP) composites were also prepared. The samples contained different volume fractions (about 15%, 25%, 35%, calculated by the thickness of each layer) of the central layers, pure P(VDF-HFP) (100%) and single layer hydantoin@BT–P(VDF-HFP) composite (0%) were denoted as S–15, S–25, S–35, S–100 and S–0.

Characterization

Transmission electron microscopy (TEM) images were obtained from a JEOL JEM–2100 instrument operated at an accelerating voltage at 200 kV, the samples were prepared by dropping the sample solutions onto carbon coated copper grids and air–

drying before measurement. Fourier-transform infrared (FT–IR) spectroscopy was performed with a Nicolet 6700 instrument over the range of 4000–450 cm^{-1} to determine the functionalization of the samples. Thermogravimetric analysis (TGA, NETZSCH STA 449) was conducted at a heating rate of 10 °C min^{-1} in a nitrogen flow (20 ml min^{-1}). Characterization of the morphology of the composites was performed by scanning electron microscopy (SEM, JSM-6390). Frequency–dependent dielectric constant, dielectric loss and electric conductivity were measured using an Agilent 4294A LCR meter with a frequency range from 1 kHz to 10 MHz. Electric displacement–electric field (*D–E*) loops and the electric breakdown strengths were measured at room temperature and 100 Hz by a Precision Premier II ferroelectric polarization tester (Radiant, Inc.), each sample was tested 4 times.

Results and Discussion

Fig. 2a displays the TEM images of the morphologies of the hydantoin@BT nanoparticles. Compared to the pristine BT particles (Fig. S1(ESI†)), the BT particles shown in Fig. 2a were coated by a polymer layer and the core–shell structure of hydantoin@BT was retained well, which was attributed to the strong bonding between BT and hydantoin epoxy resins. Fig. 2b presents the high-resolution image of an individual hydantoin@BT nanoparticle. A coherent interface between the BT particle and hydantoin resin layer can been seen in Fig. 2b, which further proves the result. The BT nanoparticles were pretreated by H_2O_2 to increase the amount of hydroxyl on the surfaces.[32] Subsequently, with the addition of hydantoin epoxy resins, a ring–opening reaction was carried out between the epoxide group of the hydantoin

resin and hydroxyl groups on the surfaces of BT nanoparticles. The addition of the curing agent dipropylenetriamine led to the cross–linking and the solidification reactions of the hydantoin epoxy resins. As a result, dense organic membranes were coated on the surfaces of BT. The FT–IR spectra of pure hydantoin epoxy resins, hydantoin@BT, BT–OH and BT is shown in Fig. 2c. An obvious broad absorption band at about 3438 cm^{-1} was appeared in the spectra, which was contributed to the stretching mode of −OH from BT–OH. After treated by H_2O_2, the −OH in BT–OH was acted as a reactive functional groups to react with the modification agents. An absorption peak at about 1702 cm^{-1} was seen in both hydantoin epoxy resins and hydantoin@BT, which was due to the C=O stretching vibrations, however, similar peak was not appeared in the curve of pure BT sample. Besides, the absorption bands at 1180 cm^{-1} was originated from the O–C stretching vibrations, which suggested that the tight chemical bond was formed between the epoxide group of hydantoin epoxy resins and –OH of BT–OH. These results strongly indicated that the hydantoin epoxy resin was successfully coated on the surface of BT nanoparticles. Fig. 2d shows the TGA curves of BT, BT–OH, hydantoin@BT and pure hydantoin epoxy resins. As can be seen that (i) there were slight weight loss below 100 °C in all of the samples, which was attributed to the deintercalation of water. (ii) The weight loss of the samples showed the sequence of BT < BT–OH < hydantoin@BT < pure hydantoin epoxy resins under 600 °C. (iii) The samples of hydantoin@BT and pure hydantoin epoxy resins exhibited a dramatic weight loss from about 350 °C to 450 °C, which was resulted from the thermal decomposition of

10

organic resin.[24] The weight residues of hydantoin@BT were attributed to BT because the weight loss of pure hydantoin epoxy resins was almost 92.4 %, thus the weight loss of hydantoin@BT nearly equaled to the amount of resin coated on the surface of BT.
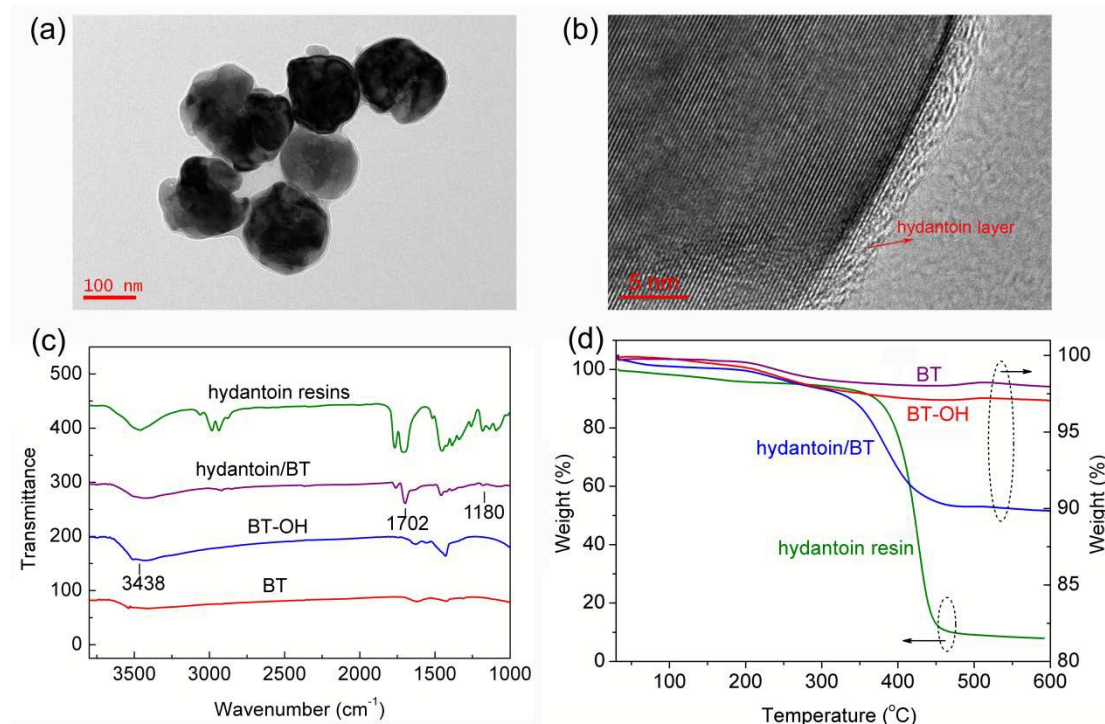
Fig. 2 (a) TEM images and (b) high-resolution TEM images of hydantoin@BT nanoparticles, (c) FT-IR spectra of the pure hydantoin epoxy resins, hydantoin@BT, BT–OH, and BT, (d) TGA curves for the BT, BT–OH, hydantoin@BT and pure hydantoin epoxy resin.

Fig. 3 shows the SEM images of the hydantoin@BT–P(VDF-HFP) composite films. As can be seen in Fig. 3a, the hydantoin@BT nanoparticles were embedded and dispersed homogeneously in the polymer matrix. Although the content of the hydantoin@BT nanoparticles was as high as 50 vol%, neglected evidence of agglomeration or defects included voids or cracks were observed in the composite.

Fig. 3b shows the SEM image of the cross-section of the hydantoin@BT–P(VDF-HFP) composite films. Since plastic deformation of the polymer matrix is inevitable in the fracture process of the composites, there are some polymer fragment would bulge in the surface, while the BT nanoparticles were still dispersed uniformly in the composites. It was indicated that the hydantoin epoxy resins shell could form strong interfacial bonding force with the P(VDF-HFP) matrix and improve the interface adhesion between the BT nanoparticles and matrix. Uniform dispersion of the BT nanoparticles in P(VDF-HFP) matrix and strong interface adhesion between the nanoparticles and matrix were beneficial to obtain high breakdown strength and energy storage density. Thus, the BT nanoparticles modified by hydantoin epoxy resin before being introduced to the polymer matrix were effective.
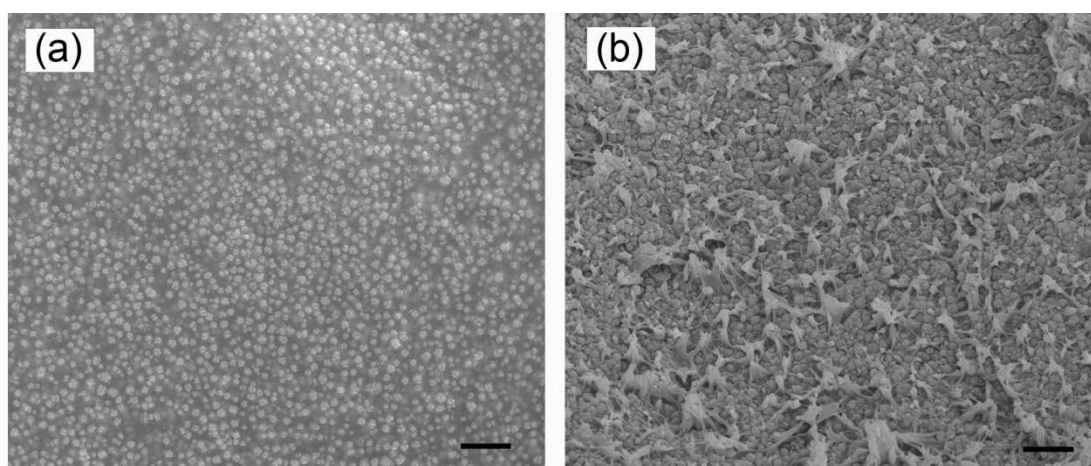
Fig. 3 SEM images of (a) top–surface and (b) cross–section of hydantoin@BT–P(VDF-HFP) composite films, scale bars are 1 μm.

The microscopic morphologies of the sandwich–structured composites were investigated by imaging the cross–section of the films. As shown in Fig. 4a–4c, the sandwich–structure and boundary lines between the central layers and neighboring

12

layers were clearly observed. The central layers in dark color were the pure P(VDF-HFP) polymer and the neighboring layers were the hydantoin@BT–P(VDF-HFP) composites. The high–magnification SEM images of sandwich–structured composites were shown in Fig. S2 (ESI†), which further exhibited the clear boundary lines between the central layers and neighboring layers and homogeneous dispersing BT particles in the composites. According to the measured thicknesses of the central layers and the neighboring layers, The volume fractions of the central pure P(VDF-HFP) layers exhibited gradient variation, which were about 35 vol%, 25 vol% and 15 vol%, as orderly shown in Fig. 4a–4c. Furthermore, all of the boundary lines were straight with negligible interlace between the pure polymer and composites, the interfaces between the central layers and neighboring layers were integrated without visible cracks and voids. In comparison, Fig. 4d shows the microscopic image of the cross–section of the single layer hydantoin@BT–P(VDF-HFP) composite. To investigate the influences of the introduced BT nanoparticles to the polymer matrix, the DSC curves of the samples obtained during the cooling scan process are presented in Fig. S3 (ESI†), which indicated that BT nanoparticles in the composites increase the crystallization temperature, which was consistent with the previous report.[19]
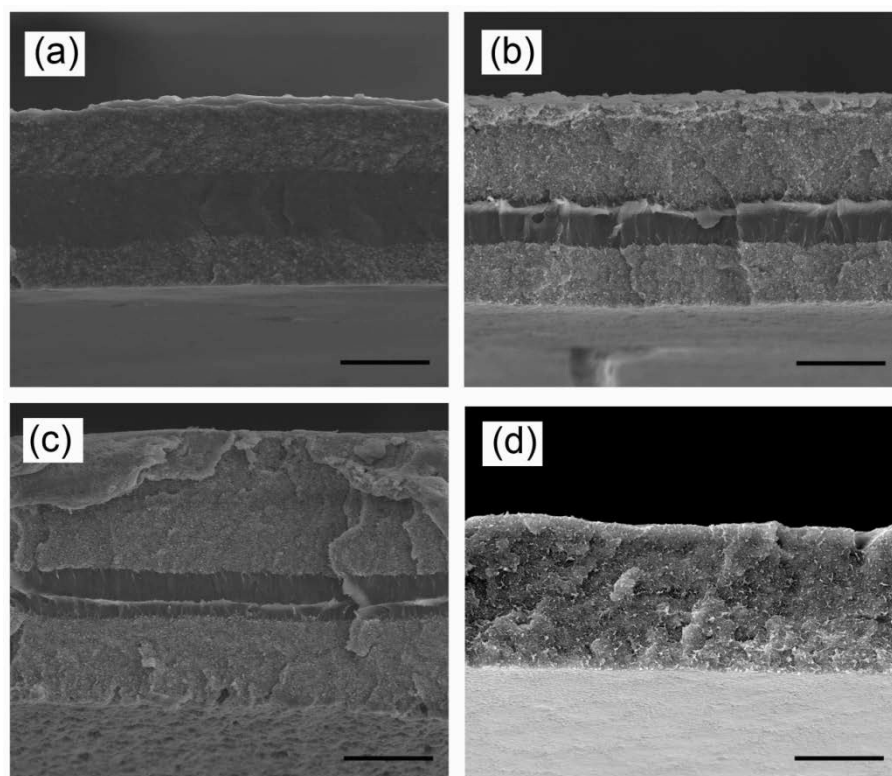
Fig. 4 Cross–section SEM morphologies of the sandwich–structured films with different volume fractions of the central layer, (a) 35 vol%, (b) 25 vol% and (c) 15 vol%. (d) Cross–section SEM image of the single layer hydantoin@BT–P(VDF-HFP) composite, scale bars are 10 μm.

The frequency dependent dielectric properties of the composites with various volume fraction of central pure P(VDF-HFP) layers are shown in Fig. 5. The frequency dependence of dielectric constants of the samples is shown is Fig. 5a. As can be seen, the dielectric constant increased with the increase of the BT loadings, and decreased with the frequency. For example, the dielectric constant of the S–15 was 27.89 at 1 kHz, and it was reduced to 15.18 at 10 MHz. The interfacial polarization plays a dominant role in the enhancement of the dielectric properties at the low frequency range. Due to the difference of the dielectric properties of the polymer layer and

14

composite layer, the interfacial polarization would take place in the polymer/composite interface, and results the enhanced dielectric constant.[26,33] The dielectric losses of the samples as a function of frequency over the range of 1 kHz to 10 MHz are shown in Fig. 4b. The dielectric losses of all the samples increased with the frequency. The increase tendency was slight in the low frequency range (below 100 kHz) and became significant in the high frequency range ($\sim > 10^5$ Hz). Due to the P(VDF-HFP) matrix, the composite films maintain a low dielectric loss at frequencies below 100 kHz. The dielectric losses of S–15, S–25 and S–35 were 0.026, 0.029 and 0.031 at 1 kHz. However, the dielectric loss of the sample S–0 without central layer was 0.043, which was obvious higher than the sandwich structured composites. The dielectric loss of the composites may be affected by the crystalline behavior of the polymer matrix. The degree of crystalline of the polymer matrix decreased with the introduction of BT nanoparticles, and led to a reduction of intermolecular force. As a result, the movement of molecular chain in the composites would be more serious with the introduction of BT nanoparticles, which is especially obvious at high frequency. Thus, the dielectric loss increased with the increase of the BT loadings at high frequency, as shown in Fig. 5b.

Fig. 5c shows the frequency dependence of the electric conductivity of the samples. The electric conductivity of the composites increased with the increase of frequency and the composites with central layers have lower electric conductivity than the hydantoin@BT–P(VDF-HFP) composite without central layer. For example, the electric conductivity of S–0 and S–35 was 2.55×10^{-6} S m^{-1} and 5.52×10^{-8} S m^{-1},

15

respectively. The results indicated that the composites with pure polymer central layer had excellent insulating property. The relatively low electric conductivity was attributed to that the pure polymer central layer in the composites prevented from the electric conduction and dipolar polarization.[22] In addition, the hydantoin shells on the surfaces of BT nanoparticles played an important role in decreasing the electric conductivities of the composites.[34, 35] Hydantoin with high insulativity was proved to be an effective modifier of ceramic fillers in polymer matrix.[31, 36] Fig. 5d displays the results of the dielectric properties of the composites as a function of the volume fraction of the central pure P(VDF-HFP) layers at 1 kHz. It exhibited that the dielectric constants decreased sharply with the increase of the volume fraction of the central layers, i.e. from 49.9 for S–0 to 6.9 for S–100. Because the BT fillers had much higher dielectric constant than the P(VDF-HFP) matrix. The content of BT decreased with the increase of the volume fraction of central layers, which led to the dielectric constants of the composites decreased. The samples with central layers and of pure P(VDF-HFP) exhibited low dielectric loss, which varied slightly with the volume fraction of the central pure P(VDF-HFP) layers. As shown in Fig. 5d, the electric conductivity of the samples with central layers was decreased with the increase of the volume fraction of the central layer. It is notably that the electric conductivity of S–35 is even lower than the pure P(VDF-HFP). The reasons may be the central insulating layer prevented the leakage current through the sample. Besides, the insulating shell on the BT nanoparticles could also restrict the migration and accumulation of the space charge within the composite.[8] However, further increase of

16

BT amount could result in defects such as the agglomerations, voids and cracks, which would lead to the increase of the electric conductivity. Thus, the electric conductivity of S–35 is the lowest and S–0, S–15 and S–25 was higher than that of the P(VDF-HFP).
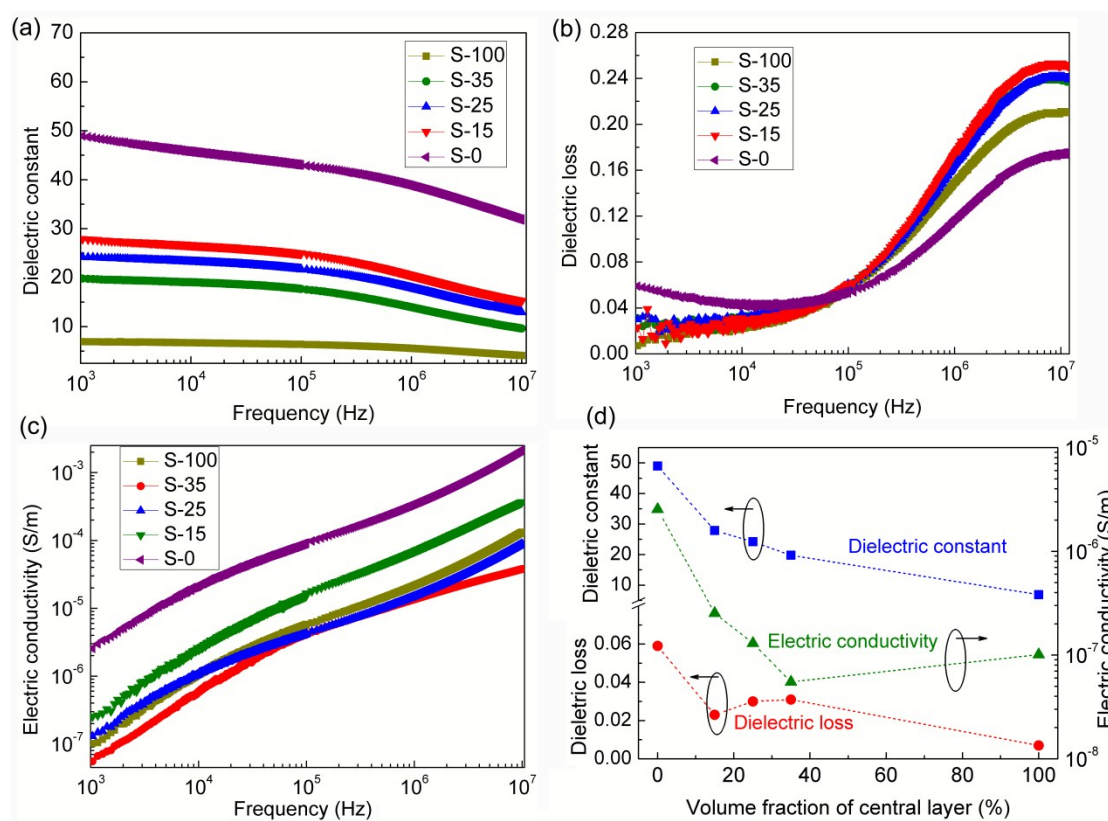
Fig. 5 Frequency dependence of (a) dielectric constant, (b) dielectric loss, and (c) electric conductivity of the samples at room temperature. (d) Dielectric constant, dielectric loss, and electric conductivity of the samples as a function of the volume fraction of the central pure P(VDF-HFP) layers at 1 kHz.

Typical D–E loops of the sandwich–structured composites, single layer composite and pure P(VDF-HFP) polymer were measured at the electric field of 160 kV mm^{-1}, which are shown in Fig. 6a. The electric displacement increased with the decrease of the

17

volume fraction of the pure polymer, and exhibited markedly increase in comparison

with the pure polymer, i.e. the maximum electric displacement was 1.52 μC cm^{-2} for

the pure P(VDF-HFP) and 4.36 μC cm^{-2} for the single layer composite. According to

the formula $D = \varepsilon_0 \varepsilon_r E$, it can be seen that the results were attributed to the increase of

the dielectric constant, which were shown in Fig. 5a. Besides, the results also

displayed that the electric displacement of the samples increased with the applied

electric field. Fig. 6b exhibits the saturated electric displacement (D_{max}) and remnant

electric displacement (D_r) of the samples with the volume fraction of central pure

polymer layers at 160 kV mm^{-1}. As shown, the D_{max} monotone decreased with the

increase of pure polymer layers. Specifically, the D_{max} of the samples of S–0, S–15,

S–25, S–35 and S–100 were 4.36 μC cm^{-2}, 4.04 μC cm^{-2}, 3.93 μC cm^{-2}, 3.60 μC cm^{-2}

and 1.52 μC cm^{-2}. The D_r of the samples exhibited a similar rule, which were 1.40 μC

cm^{-2}, 1.15 μC cm^{-2}, 0.86 μC cm^{-2}, 0.79 μC cm^{-2} and 0.07 μC cm^{-2}. It was known that

the high remnant polarization would lessen the discharging energy density. Thus,

these results indicated that the samples with central layer would have higher

discharged energy density.
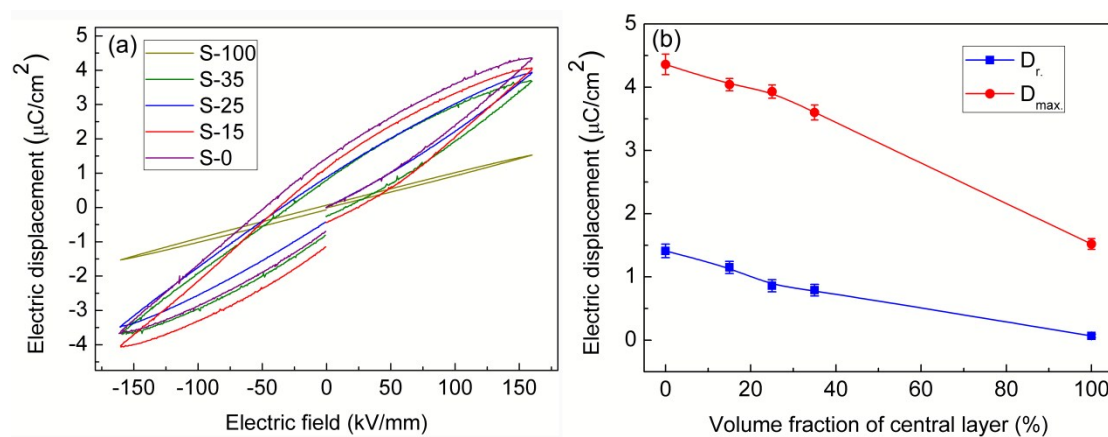
Fig. 6 (a) *D–E* loops of the samples at the applied electric field of 160 kV mm^{-1}. (b)

Saturated electric displacement and remnant electric displacement with the volume

fraction of the central layers.

Table 1. The electric performances of the sandwich–structured composites, the pure

P(VDF-HFP) and single layer composite.

No.	E_b (kV/mm)	D^*_{max} (μC/cm^2)	c (μC/cm^2)	U_{dis} (J/cm^3)
S–100	360	2.58	0.11	3.74
S–35	315	4.75	1.07	5.22
S–25	280	6.10	1.72	5.12
S–15	262	7.68	3.19	4.32
S–0	187	4.36	1.44	2.32

The ideal case is simultaneously enhanced electric displacement and breakdown

strength. Therefore, it is necessary to deeply discuss the electric displacement and

breakdown strength to fully characterize the energy storage capability of the

composites. The effective electric displacement (the minus of the electric

displacement (D^*_{max}) and remnant electric displacement (D^*_r) at the maximum electric

field) and breakdown strength with the volume fractions of central layers are

presented in Fig. 7 and the specific results are shown in table 1. As can be seen, the

D^*_{max} was increased from 4.36 μC cm^{-2} for S–0 to 6.10 μC cm^{-2} for S–25 and 4.75μC

cm^{-2} for S–35 with an enhancement of approximately 40 % and 11 %, respectively.

The results of breakdown strength of the composites are showed in Fig. 7b. As can be

seen, the breakdown strength of the composites with central layers was sharply

enhanced. The breakdown strength of S–0 was only 187 kV mm^{-1}, while the sample

of S–25 and S–35 with central layer were 280 kV mm^{-1} and 315 kV mm^{-1}, which were increased by approximately 50 % and 68 %, respectively. These results revealed the distinctive advantage of the sandwich–structured composites in enhancing the electric displacement and the dielectric breakdown compared with the single layer composite, which were exhibited remarkably in the frame area (see Fig. 7). Due to the simultaneously enhanced E_b and D, the discharged energy density (U_{dis}, extracted from the electric D–E loops on the basis of definition $U_{dis} = \int_{D_r}^{D_{max}} EdD$) [37-39] of S–25 and S–35 were significantly increased to 5.22 J cm^{-3} and 5.12 J cm^{-3} , which were much larger than the U_{dis} of 2.35 J cm^{-3} for the hydantoin@BT–P(VDF-HFP) single layer composite.

The significantly enhanced breakdown strength may be attributed to several reasons, which include (i) the high electric field was redistributed among the different layers, which led to local electric field was much higher than its intrinsic breakdown strength in the BT–P(VDF-HFP) layers. As a result, the outer layers would form incomplete breakdown. (ii) The incomplete breakdown channels could share the accumulated electric energy in the outer layers, which was beneficial to the alleviation of the dielectric stress and avoided the complete breakdown of the multilayer composites.[2, 3, 40, 41]
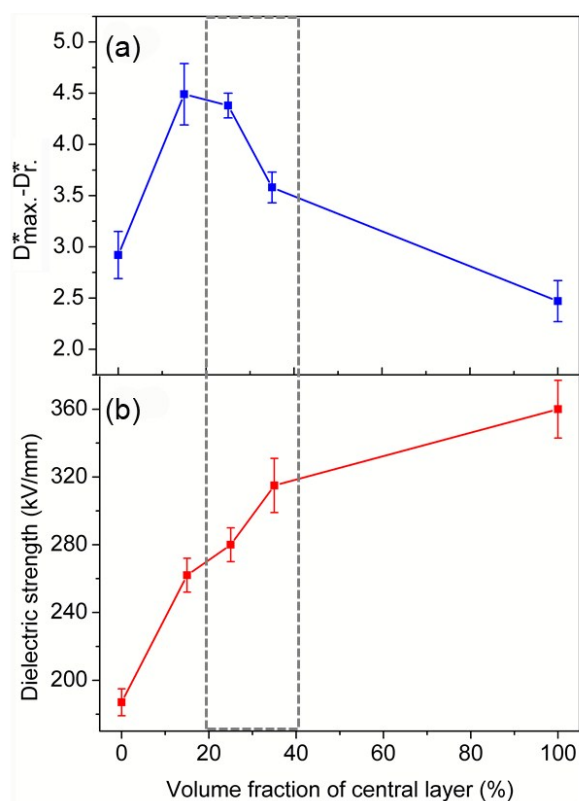
Fig. 7 (a) Maximum electric displacement and (b) breakdown strength of the composites vary with the volume fractions of the central layers.

Fig. 8a shows the energy densities of the sandwich–structured composites, single layer composite (S–0) and pure P(VDF-HFP) (S–100) with the electric field. It is shown that the sandwich–structured composites have higher U_{dis} compared with the pure P(VDF-HFP). The U_{dis} of the S–15, S–25 and S–35 samples were 4.32 J cm^{-3}, 5.12 J cm^{-3} and 5.22 J cm^{-3}. The U_{dis} of the S–35 was increased by 125% compared with the single layer sample S–0 (2.32 J cm^{-3}), and was much greater than the biaxially oriented polypropylene (BOPP) (1.2 J cm^{-3} at 640 kV mm^{-1}).[15] The D–E loops of the sandwich–structured samples are measured with the electric field, which are shown in Fig. S4 (ESI†). According to the equation $\eta=U_{dis}/U_{sto}$ (η and U_{sto}

21

represents the energy efficiency and stored energy densities, respectively), the η calculated from the D–E loops of all the samples at 160 kV mm^{-1} were listed in Fig.8b. As can be seen, the pure P(VDF-HFP) sample showed the maximum η of 89.46%, and the η decreased with the introduce of BT nanoparticles. Due to the relatively low remnant polarization, the S–25 sample had the highest η among the sandwiched composites, which was attributed to the relatively small D_r^* of the sample.
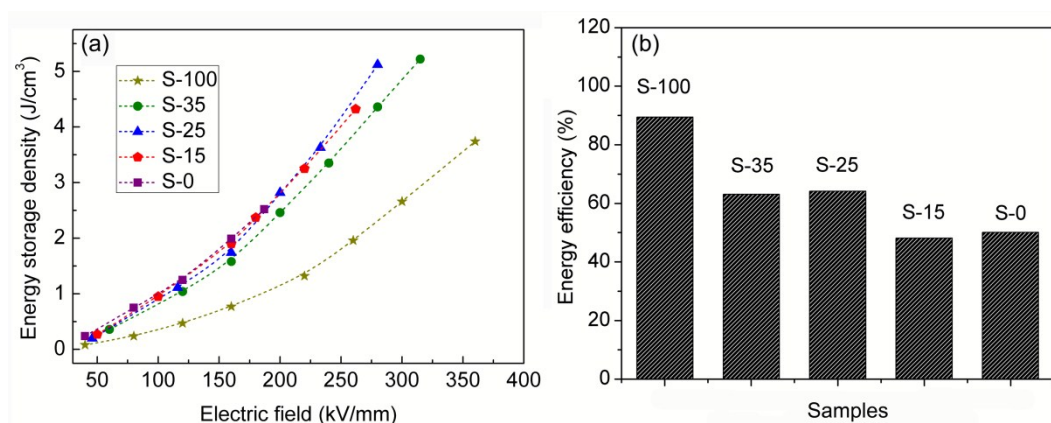
Fig. 8 (a)Discharged energy densities of the samples with the electric field. (b) Energy efficiency of the sample at the electric field of 160 kV mm^{-1}.

Conclusions

A group of sandwich–structured hydantoin@BT–P(VDF-HFP) composites with various volume fraction of central pure P(VDF-HFP) layer were produced. Due to central buffered layers, the sandwich–structured composites exhibited significantly superiority on enhancing the dielectric strength and U_{dis} compared with the single layer composite. The sample of S–35 exhibited U_{dis} of 5.22 J cm^{-3} with a dielectric strength of 315 kV mm^{-1}, which was 125 % larger than the single layer composite

(2.32 J cm^{-3} at 187 kV mm^{-1}) and more than 4 times of the BOPP (1.2 J cm^{-3} at 640 kV mm^{-1}). Meanwhile, the sandwich–structured composites of S–15, S–25 and S–35 displayed low dielectric losses of 0.026, 0.029 and 0.031 at 1 kHz. It was demonstrated that the sandwich–structured composites exhibited excellent endurance of high electric field and high energy storage capacity, which exceeded the sum of the single constituents of the sandwich-structured composites.

Electronic Supporting Information

Dielectric constants and breakdown strength of single layer of P(VDF-HFP) composites with different BT loadings. TEM and SEM images of the pure BT particles. High–magnification SEM images of the sandwich–structured composites. DSC curves of the samples during the heating cycle at a rate of 10 ^{o}C min^{-1} under N$_2$ atmosphere. *D–E* loops of the samples at maximum electric field.

Acknowledgements

References

1   V. K. Thakur, G. Ding, J. Ma, P. S. Lee and X. Lu, *Adv. Mater.*, 2012, **24**, 4071-4096.

2   P. Hu, J. Wang, Y. Shen, Y. Guan, Y. Lin and C.-W. Nan, *J. Mater. Chem. A*, 2013, **1**, 12321-12326.

3   P. Hu, Y. Shen, Y. Guan, X. Zhang, Y. Lin, Q. Zhang and C.-W. Nan, *Adv. Funct. Mater.*, 2014, **24**, 3172-3178.

4   H. Tang, Y. Lin and H. A. Sodano, *Adv. Energy Mater.*, 2013, **3**, 451-456.

5   S. Liu, J. Zhai, J. Wang, S. Xue and W. Zhang, *ACS Appl. Mater. Interfaces*, 2014, **6**, 1533-1540.

6   L. Wu, X. Wang, H. Gong, Y. Hao, Z. Shen and L. Li, *J. Mater. Chem. C*, 2015, **3**, 750-758.

7   H. Tang, Y. Lin and H. A. Sodano, *Adv. Energy Mater.*, 2012, **2**, 469-476.

8   K. Yang, X. Huang, Y. Huang, L. Xie and P. Jiang, *Chem. Mater.*, 2013, **25**, 2327-2338.

9   V. K. Thakur, E. J. Tan, M.-F. Lin and P. S. Lee, *J. Mater. Chem.*, 2011, **21**, 3751-3759.

10   V. K. Thakur, M.-F. Lin, E. J. Tan and P. S. Lee, *J. Mater. Chem.*, 2012, **22**, 5951-5959.

11   V. K. Thakur, E. J. Tan, M.-F. Lin and P. S. Lee, *Polym. Chem.*, 2011, **2**, 2000-2009.

12   M.-F. Lin, V. K. Thakur, E. J. Tan and P. S. Lee, *J. Mater. Chem.*, 2011, **21**,

16500-16504.

13   M.-F. Lin, V. K. Thakur, E. J. Tan and P. S. Lee, *RSC Adv.*, 2011, **1**, 576-578.

14   J. Li, J. Claude, L. E. Norena-Franco, S. Il Seok and Q. Wang, *Chem. Mater.*, 2008, **20**, 6304-6306.

15   H. Tang and H. A. Sodano, *Nano Lett.*, 2013, **13**, 1373-1379.

16   Z. D. Liu, Y. Feng and W. L. Li, *RSC Adv.*, 2015, **5**, 29017-29021.

17   P. Hu, Y. Song, H. Liu, Y. Shen, Y. Lin and C.-W. Nan, *J. Mater. Chem. A*, 2013, **1**, 1688-1693.

18   J. Li, S. I. Seok, B. Chu, F. Dogan, Q. Zhang and Q. Wang, *Adv. Mater.*, 2009, **21**, 217-221.

19   D. Yu, N.-X. Xu, L. Hu, Q.-l. Zhang and H. Yang, *J. Mater. Chem. C*, 2015, **3**, 4016-4022.

20   S. Liu, S. Xue, W. Zhang, J. Zhai and G. Chen, *J. Mater. Chem. A*, 2014, **2**, 18040-18046.

21   L. Xie, X. Huang, K. Yang, S. Li and P. Jiang, *J. Mater. Chem. A*, 2014, **2**, 5244-5251.

22   Z.-M. Dang, H.-Y. Wang and H.-P. Xu, *Appl. Phys. Lett.*, 2006, **89**, 112902.

23   K. Yang, X. Huang, M. Zhu, L. Xie, T. Tanaka and P. Jiang, *ACS Appl. Mater. Interfaces*, 2014, **6**, 1812-1822.

24   D. Wang, T. Zhou, J.-W. Zha, J. Zhao, C.-Y. Shi and Z.-M. Dang, *J. Mater. Chem. A*, 2013, **1**, 6162-6168.

25   D. Wang, Y. Bao, J.-W. Zha, J. Zhao, Z.-M. Dang and G.-H. Hu, *ACS Appl.*

Mater. Interfaces, 2012, **4**, 6273-6279.

26   L. L. Sun, B. Li, Y. Zhao, G. Mitchell and W. H. Zhong, *Nanotechnology*, 2010, **21**.

27   K. Yu, Y. Niu, Y. Zhou, Y. Bai and H. Wang, *J. Am. Ceram. Soc.*, 2013, **96**, 2519-2524.

28   P. Kim, N. M. Doss, J. P. Tillotson, P. J. Hotchkiss, M.-J. Pan, S. R. Marder, J. Li, J. P. Calame and J. W. Perry, *ACS Nano*, 2009, **3**, 2581-2592.

29   S. Liu and J. Zhai, *J. Mater. Chem. A*, 2015, **3**, 1511-1517.

30   V. K. Thakur, J. Yan, M.-F. Lin, C. Zhi, D. Golberg, Y. Bando, R. Sim and P. S. Lee, *Polym. Chem.*, 2012, **3**, 962-969.

31   H. Luo, D. Zhang, C. Jiang, X. Yuan, C. Chen and K. Zhou, *ACS Appl. Mater. Interfaces*, 2015, **7**, 8061-8069.

32   L. Xie, X. Huang, C. Wu and P. Jiang, *J. Mater. Chem.*, 2011, **21**, 5897-5906.

33   W. Benhadjala, I. Bord-Majek, L. Bechou, E. Suhir, M. Buet, F. Rouge, V. Gaud, B. Plano and Y. Ousten, *Appl. Phys. Lett.*, 2012, **101**, 142901.

34   X. Huang and P. Jiang, *Adv. Mater.*, 2015, **27**, 546-554.

35   M. Zhu, X. Huang, K. Yang, X. Zhai, J. Zhang, J. He and P. Jiang, *ACS Appl. Mater. Interfaces*, 2014, **6**, 19644-19654.

36   C. Min, D. Yu, J. Cao, G. Wang and L. Feng, *Carbon*, 2013, **55**, 116-125.

37   B. Chu, X. Zhou, K. Ren, B. Neese, M. Lin, Q. Wang, F. Bauer and Q. M. Zhang, *Science*, 2006, **313**, 334-336.

38   X. Hao, J. Zhai and X. Yao, *J. Am. Ceram. Soc.*, 2009, **92**, 1133-1135.

39   K. Yang, X. Huang, L. Xie, C. Wu, P. Jiang and T. Tanaka, *Macromol. Rapid Commun.*, 2012, **33**, 1921-1926.

40   D. P. Agoris, I. Vitellas, O. S. Gefle, S. M. Lebedev and Y. P. Pokholkov, *J. Phys. D-Appl. Phys.*, 2001, **34**, 3485-3491.

41   L. A. Fredin, Z. Li, M. T. Lanagan, M. A. Ratner and T. J. Marks, *Adv. Funct. Mater.*, 2013, **23**, 3560-3569.

Table of contents:

The dielectric strength and discharged energy density are largely enhanced in the

sandwich-structured hydantoin@$BaTiO_3$–P(VDF-HFP) composites.

28